

Modeling Microtubule-Based Transport and Anchoring of mRNA*

Maria-Veronica Ciocanel[†], Bjorn Sandstede[‡], Samantha P. Jeschonek[§], and
Kimberly L. Mowry[§]

Abstract. Localization of messenger RNA (mRNA) at the vegetal cortex plays an important role in the early development of *Xenopus laevis* oocytes. While it is known that molecular motors are responsible for the transport of mRNA cargo along microtubules to the cortex, the mechanisms of localization remain unclear. We model cargo transport along microtubules using partial differential equations with spatially dependent rates. A theoretical analysis of reduced versions of our model predicts effective velocity and diffusion rates for the cargo and shows that randomness of microtubule networks enhances effective transport. A more complex model using parameters estimated from fluorescence microscopy data reproduces the time and spatial scales of mRNA localization observed in *Xenopus* oocytes, corroborates experimental hypotheses that anchoring may be necessary to achieve complete localization, and shows that anchoring of mRNA complexes actively transported to the cortex is most effective in achieving robust accumulation at the cortex.

Key words. intracellular transport, microtubules, anchoring, long-time dynamics, reaction-diffusion model

AMS subject classifications. 35B40, 35K57, 92C15, 92C40

DOI. 10.1137/18M1186083

1. Introduction. The cellular cytoskeleton is key in ensuring the dynamic transport and localization of many different RNAs, proteins, and vesicles. Polarized networks of microtubule tracks often provide the basis for directional transport of various intracellular cargoes that regulate essential processes such as cell division, cell motility, and embryogenesis in various organisms. In many of these biological processes, the mechanisms underlying the time and spatial scales of protein and RNA localization are not known, and a better understanding of the impact of the microtubule geometry on transport processes is required.

One example where the cytoskeleton plays a key role in transport is messenger RNA (mRNA) localization to the vegetal cortex during oogenesis of the frog *Xenopus laevis*. The asymmetric distribution of Vg1 mRNA in the vegetal cytoplasm of the frog oocyte is critical for correct embryonic patterning in this organism, and similar localization processes occur in many other biological systems [14, 36]. The molecular motors kinesin and dynein are responsible for the transport of mRNA cargo along polarized microtubules to the vegetal

*Received by the editors May 8, 2018; accepted for publication (in revised form) October 26, 2018; published electronically December 18, 2018.

<http://www.siam.org/journals/siads/17-4/M118608.html>

Funding: The work of the first author was supported by the Mathematical Biosciences Institute and the NSF under grant DMS 1440386. The work of the second author was supported by NSF grants 1714429 and 1740741. The work of the fourth author was supported by NSF grant R01GM071049.

[†]Mathematical Biosciences Institute, The Ohio State University, Columbus, OH 43210 (ciocanel.1@mbi.osu.edu).

[‡]Division of Applied Mathematics, Brown University, Providence, RI 02912 (Bjorn.Sandstede@brown.edu).

[§]Department of Molecular Biology, Cell Biology and Biochemistry, Brown University, Providence, RI 02912 (Samantha_Jeschonek@brown.edu, kimberly_mowry@brown.edu).

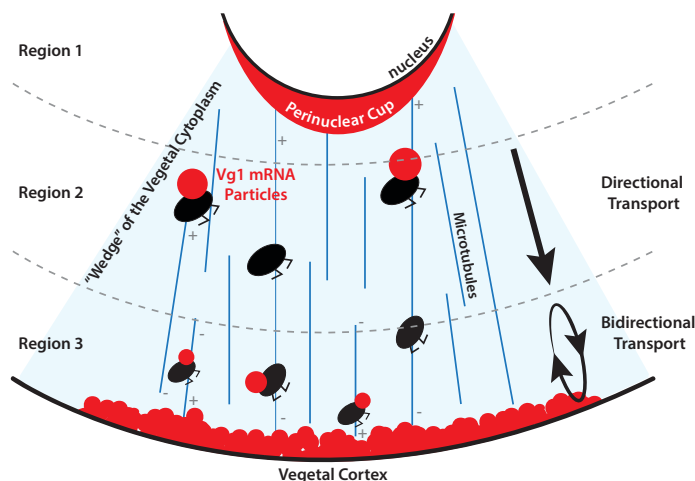


Figure 1. Schematic of mRNA localization in the vegetal cytoplasm of a *Xenopus* oocyte. mRNA cargoes (red) are transported by motor proteins (black) along polarized microtubule filaments (blue lines) towards the vegetal cortex. The vegetal cytoplasm is schematically divided into three regions where transport parameters have been found to differ [10].

cortex of the *Xenopus* oocyte [17,37] (see Figure 1). Dynein moves cargo to the minus ends of microtubules and is hypothesized to contribute to directional transport towards the cortex in the upper cytoplasm (Regions 1 and 2 in Figure 1), while kinesin moves cargo to the plus ends of microtubules and may be involved in bidirectional transport in the lower cytoplasm (Region 3 in Figure 1) [17]. Despite these experimental insights, the mechanisms of localization remain unclear. In particular, experiments suggest that mRNA is anchored at the cortex [1,41,56], but it is not known whether this is necessary for mRNA localization. Our goal is therefore to take into account the microtubules in modeling the mRNA localization process in *Xenopus* oocytes and to provide insights into the mechanisms behind the time and spatial scales of localization and anchoring in this developmental process.

In our previous work [10] (see also [41]), we used linear transport models coupled with parameter estimation and analysis to determine diffusion coefficients, motor speeds, and switching rates for the transitions on and off microtubules for dynamic populations of mRNA in *Xenopus* oocytes using FRAP (fluorescence recovery after photobleaching) data [17]. The analysis there allowed us to suggest differences in transport efficiency of mRNA in different regions of the oocyte cytoplasm. These constant transition rate models are useful in modeling dynamics on the short timescale of the FRAP experiments; however, they cannot provide insights onto the longer timescale of mRNA localization, where the transport directionality depends on the complex microtubule cytoskeleton. Here we build on the models and parameter estimates in [10] and incorporate the spatial microtubule networks through spatially dependent transition rates. We carry out a large-time analysis of reaction-advection-diffusion transport models on parallel filaments using Fourier expansion and Lyapunov–Schmidt reduction and extend existing effective transport results [8] to general systems with an arbitrary number of dynamical states and under no assumptions on the scales of the parameters or on

the filament density. Our findings and predictions for the dynamics of mRNA in *Xenopus* can be summarized as follows:

- An inhomogeneous or random microtubule cytoskeleton leads to a more effective spread of diffusing cargo than uniformly spaced filaments.
- Anchoring may be necessary to achieve complete localization and to reproduce the timescales of mRNA localization observed in *Xenopus* oocytes.
- Anchoring of mRNA actively delivered to the cortex is most effective in achieving robust localization.
- mRNA anchoring may be enhanced by mRNA already anchored at the cortex.

The models we propose do not explicitly account for the polarity (plus/minus ends) of the microtubules or for the specific motor species carrying out the transport in each region. Instead, we assume that this information is embedded in the different kinetic parameters estimated for each region of the *Xenopus* oocyte cytoplasm (see Figure 1) in [10]. The models proposed do, however, account for the geometry and orientation of the microtubule filaments in the domain, which we henceforth refer to as the microtubule structure.

Previous models for the transport of RNA and proteins along realistic cellular cytoskeleton geometries have been proposed to study cell polarization in the mating budding yeast and neural growth cones [8, 23], as well as mRNA localization in *Drosophila* oocytes [48]. These studies use partial differential equations and stochastic models to represent switching between a diffusion state and a state of active transport along directed microtubule networks. Analytically, the transport properties of the particles in these dynamic models (effective velocity and diffusion) are determined in [8] using the quasi-steady-state reduction method [7, 39, 40], under assumptions of very fast switching rates and very slow diffusion relative to the motor protein velocities. In many systems, however, these assumptions on the parameters of the dynamics are unlikely to be biologically relevant. For instance, our parameter estimation based on FRAP microscopy data in [10] revealed that diffusion coefficients may be larger in magnitude than motor speeds in Vg1 mRNA localization during *Xenopus laevis* oogenesis. Our theoretical results therefore extend the analysis of transport models with parallel filaments to general systems with arbitrary parameters.

In addition to the applicability of this analysis to many biological systems where transport relies on parallel filaments, our derived effective transport predictions contain additional terms in the predicted diffusivity, which can be numerically evaluated to show that nonuniform cytoskeleton networks lead to faster transport and a wider spread of the particles modeled. This observation motivates the use of accurate microtubule structures with biologically informed orientations as in [18, 48]. Evidence for variable microtubule arrangements and the resulting cytoplasmic streaming has been previously found in *Drosophila* oocytes using quantification of Particle Image Velocimetry in kinesin-dependent streaming [18]. The studies [18, 49] also found that a disordered network of filaments may balance active transport with advective fluid flows and thus aid in targeted localization by allowing for fluctuations of motor-dependent flows. More recently, the study [48] tested the localization of two types of mRNA at a late stage in *Drosophila* oogenesis using a two-state model of the dynamics and standard values for key dynamic parameters. We focus on a more complex four-state model for mRNA transport and localization in the frog *Xenopus laevis* [10] coupled to a random but radially biased microtubule network informed from experimental observations in [4, 17, 19, 37]. This model

accounts for the bidirectional movement of the particles driven by kinesin and dynein motors, both of which have been found to contribute to mRNA localization in this system [10, 17, 37]. In this model, parameters such as diffusion coefficients, motor velocities, and transition rates depend on the location in the cytoplasm [10], and we use estimates of these parameters based on the experimental data in [17].

Our approach allows us to assess transport timelines in mRNA localization and to provide insight into additional mechanisms such as anchoring, which are challenging to study experimentally in *Xenopus* oocytes. In particular, anchoring of mRNA at the target destination in developing oocytes and embryos is not fully understood, with some studies suggesting an actin-dependent mechanism at the cortex [1, 56] and proposing a role for mediating factors and vesicles [1, 24, 30, 56, 57]. In *Drosophila* oocytes, [50] proposes a microtubule-independent anchoring mechanism of bicoid mRNA at the anterior pole, while [11] suggests that apical anchoring of RNA is microtubule-dependent in blastoderm embryos. Despite the different experimental findings in different organisms or stages of development, the numerical framework we propose provides a way to investigate these questions and suggests that active delivery (likely by molecular motors) is necessary for the observed timescale of proper vegetal localization and that an anchoring mechanism (potentially dependent on mRNA already localized) is required for robust accumulation of mRNA at the cortex in *Xenopus* oocytes.

2. Quantifying transport along microtubule networks using PDE models.

2.1. Model formulation. Similar to [8, 23], we consider a model of the dynamics of mRNA particles where transport is restricted to given microtubule structures. Particles can switch between a freely diffusing state and a transport state for motor-cargo complexes with velocity $\mathbf{V}(\theta)$. The direction of transport θ is determined by the orientation of the cytoskeletal filament bound to the complex at location (x, y) (see Figure 2(A)). We assume as in [8] that there is a density $\rho(\mathbf{r}, \theta)$ of filaments with a given orientation θ at each location $\mathbf{r} = (x, y)$. Particle

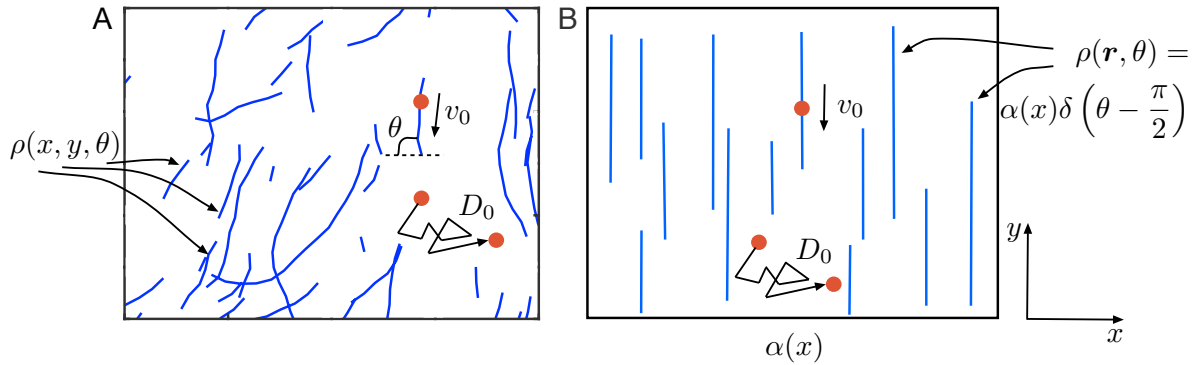


Figure 2. (A) Illustration of a microtubule structure with density ρ (blue lines). Particles (red dots) can either be transported with velocity v_0 along microtubule filaments, or freely diffuse in the cytoplasm with diffusion coefficient D_0 . The density of microtubules at location (x, y) with orientation θ is given by $\rho(x, y, \theta)$. (B) Illustration of a parallel microtubule structure with density $\rho(\mathbf{r}, \theta) = \alpha(x)\delta(\theta - \pi/2)$ (blue lines). Here particle transport can occur with velocity v_0 straight down on parallel microtubule filaments.

movement is then modeled using the equations

$$(1) \quad \begin{aligned} \frac{\partial p(\mathbf{r}, \theta, t)}{\partial t} &= -\mathbf{V}(\theta) \cdot \nabla p(\mathbf{r}, \theta, t) - \beta p(\mathbf{r}, \theta, t) + \alpha \rho(\mathbf{r}, \theta) p_0(\mathbf{r}, t), \\ \frac{\partial p_0(\mathbf{r}, t)}{\partial t} &= D \nabla^2 p_0(\mathbf{r}, t) + \beta \int_0^\pi p(\mathbf{r}, \theta, t) d\theta - \alpha \bar{\rho}(\mathbf{r}) p_0(\mathbf{r}, t), \end{aligned}$$

where $p_0(\mathbf{r}, t)$ denotes the concentration of diffusing particles at position $\mathbf{r} = (x, y)$ at time t , and $p(\mathbf{r}, \theta, t)$ is the concentration of particles bound to a microtubule at location \mathbf{r} and moving with velocity $\mathbf{V}(\theta)$ [8]. Here $\bar{\rho}(\mathbf{r}) = \int_0^\pi \rho(\mathbf{r}, \theta) d\theta$ is the availability of filaments at a certain location averaged over all orientations θ , β corresponds to the transition rate from the transport state to the diffusing state, and α corresponds to the transition rate from diffusion to transport.

Our parameter estimation results in [10] indicate that diffusion and binding rate parameters can vary throughout the cytoplasm and that neither diffusion nor binding dominates the dynamics. This suggests that existing approaches to analyze equations (1), which assume very fast switching rates and slow diffusion compared to typical motor velocities [8], do not hold in the case of mobility of mRNA in *Xenopus* oocytes. In particular, the quasi-steady-state approximation in [8] does not apply in this setting, and we therefore proceed with different analytical methods that do not require assumptions on the magnitude of the system parameters. To simplify the analysis, we start by considering the case where filaments are oriented parallel to each other. As in [8], we let the density of filaments vary with spatial dimension x via

$$\rho(\mathbf{r}, \theta) = \alpha(x) \delta(\theta - \pi/2),$$

where we recall that $\mathbf{r} = (x, y)$ (see Figure 2(B)). The function $\alpha(x)$ reflects the assumption that the parallel filaments have a density proportional to the concentration of surface signaling molecules on the membrane, as in [8]. Evidence for such a relationship is found in the distribution of microtubules in neuron growth cones, where growing microtubule ends are regulated by and bind with GABA receptors on the membrane [5]. Thus, the function $\alpha(x)$ would be given in the form of a piecewise constant step function that takes the value zero in regions with no microtubules and a strictly positive value on microtubules.

Letting $\bar{p}(\mathbf{r}, t) = \int_0^\pi p(\mathbf{r}, \theta, t) d\theta$ and noting that $\bar{\rho} = \int_0^\pi \rho(\mathbf{r}, \theta) d\theta = \alpha(x)$, we obtain the equations

$$(2) \quad \begin{aligned} \frac{\partial \bar{p}(\mathbf{r}, t)}{\partial t} &= v_0 \mathbf{e}_y \cdot \nabla \bar{p}(\mathbf{r}, t) - \beta \bar{p}(\mathbf{r}, t) + \alpha(x) p_0(\mathbf{r}, t), \\ \frac{\partial p_0(\mathbf{r}, t)}{\partial t} &= D \nabla^2 p_0(\mathbf{r}, t) + \beta \bar{p}(\mathbf{r}, t) - \alpha(x) p_0(\mathbf{r}, t) \end{aligned}$$

for the concentrations of particles in the two states that correspond to active transport and diffusion, respectively.

To account for bidirectional movement, more complex models with additional dynamic states would be of interest. For instance, we found in [10] that a model with four dynamical states that account for movement up along filaments, movement down along filaments, diffusion, and pausing (see equations (38) below) may be more accurate for describing the

mRNA dynamics in different regions of the cytoplasm. Therefore, the theoretical result in the next section is obtained for general systems of linear advection-reaction-diffusion partial differential equations with spatially dependent transition rates.

2.2. Main result. To determine the asymptotic behavior of particles restricted to transport on parallel filaments, we calculate their effective velocity and diffusion at large time. We consider the general case of an arbitrary number of particle populations that can move bidirectionally on the microtubule tracks, diffuse or pause when off-track, and switch between these states at given rates; more precisely, we consider the system of advection-reaction-diffusion equations given by

$$(3) \quad \frac{d}{dt} \begin{pmatrix} u_0 \\ u_1 \\ \dots \\ u_n \end{pmatrix} = D \nabla^2 \begin{pmatrix} u_0 \\ u_1 \\ \dots \\ u_n \end{pmatrix} + C \frac{d}{dy} \begin{pmatrix} u_0 \\ u_1 \\ \dots \\ u_n \end{pmatrix} + A(x) \begin{pmatrix} u_0 \\ u_1 \\ \dots \\ u_n \end{pmatrix}, \quad \nabla = \begin{pmatrix} \partial_x \\ \partial_y \end{pmatrix},$$

where $(x, y) \in [0, 1] \times \mathbb{R}$, $D = \text{diag}(d_j)$, $C = \text{diag}(c_j)$, together with the boundary conditions

$$(4) \quad \frac{\partial u_j}{\partial x}(x=0, y, t) = \frac{\partial u_j}{\partial x}(x=1, y, t) = 0,$$

for all states j with $d_j > 0$. The variables $u_j \in \mathbb{R}$ model concentrations of particles that diffuse and are transported along a cytoskeleton of parallel vertical filaments. The diagonal matrices C and D contain the speeds c_j and diffusion coefficients d_j , respectively, in each state, while the transitions between states are described by the reaction-rate matrix $A(x)$. The x -dependence of the reaction-rate matrix $A(x)$ accounts for the availability of microtubules at a certain location. Finally, we separate the solution vector \mathbf{u} into vectors for diffusing and nondiffusing populations, so that $\mathbf{u} = (\mathbf{u}_1, \mathbf{u}_2)$ with \mathbf{u}_1 corresponding to states where $d_j > 0$, and introduce the space $\mathcal{X} := \{\mathbf{u}_1 \in H^2([0, 1]) : \frac{\partial u_1}{\partial x}|_{x=0} = \frac{\partial u_1}{\partial x}|_{x=1} = 0\} \times \{\mathbf{u}_2 \in L^2([0, 1])\}$.

Theorem 2.1. Assume that C and D are diagonal matrices and that the entries of D are nonnegative. We also assume that $A(x) = (a_{ij}(x))_{i,j=1,\dots,n}$ and that each entry $a_{ij}(x)$ satisfies $\inf\{|a_{ij}(x)|; x \in [0, 1], a_{ij}(x) \neq 0\} > 0$. Finally, we assume that the operators $L_0 := D\partial_x^2 + A(x)$ and $L_0^* := D\partial_x^2 + A(x)^*$ posed on $L^2([0, 1])$ with domain \mathcal{X} each have a one-dimensional null space, spanned by $\mathbf{u}_0(x)$ and $\psi_0(x)$, respectively, and that their remaining eigenvalues have real part strictly less than zero. Let $\mathbf{u}(\mathbf{r}, t)$ denote the solution of (3) with initial condition given by a Gaussian initial condition for each u_j ; then, as $t \rightarrow \infty$, the solution has the asymptotic Gaussian form

$$\mathbf{u}(\mathbf{r}, t) = \frac{a}{\sqrt{2\pi\sigma_{\text{eff}}t}} e^{\frac{(y+v_{\text{eff}}t)^2}{2\sigma_{\text{eff}}t}} \mathbf{u}_0(x)$$

for some $a \in \mathbb{R}$. Furthermore, the effective velocity v_{eff} and the effective diffusion coefficient σ_{eff} of the particles in the direction y of transport are given by

$$(5) \quad v_{\text{eff}} = \frac{\langle \psi_0, C\mathbf{u}_0 \rangle}{\langle \psi_0, \mathbf{u}_0 \rangle},$$

$$(6) \quad \sigma_{\text{eff}} = \frac{\langle \psi_0, D\mathbf{u}_0 \rangle}{\langle \psi_0, \mathbf{u}_0 \rangle} + \frac{\langle \psi_0, C\mathbf{w}_0(x) \rangle}{\langle \psi_0, \mathbf{u}_0 \rangle},$$

where $\langle f(x), g(x) \rangle = \int_0^1 f(x)g(x)dx$, and \mathbf{w}_0 is the unique solution of

$$(7) \quad L_0 \mathbf{w}_0(x) + C \mathbf{u}_0(x) - \frac{\langle \boldsymbol{\psi}_0, C \mathbf{u}_0 \rangle}{\langle \boldsymbol{\psi}_0, \mathbf{u}_0 \rangle} \mathbf{u}_0(x) = 0, \quad \mathbf{w}_0 \in \mathcal{X}.$$

We prove Theorem 2.1 in section 2.5.

2.3. Remarks on Theorem 2.1. To motivate the assumptions for Theorem 2.1 and show their broad applicability, we provide the following remarks.

Remark 1. If matrix $A(x)$ models conservation of particles, then $A(x)$ is a quasi-positive irreducible matrix. The Perron–Frobenius theory for quasi-positive matrices then ensures that the zero eigenvalue has algebraic multiplicity 1 and that all other eigenvalues of $A(x)$ have strictly negative real part for each x . The linear operator $L_0 = D\partial_x^2 + A(x)$ can only add diagonal entries to matrix $A(x)$ and is therefore also quasi-positive and irreducible. The real part of all other eigenvalues is thus guaranteed to be less than zero, and the assumption in the theorem is satisfied.

Remark 2. Note that in the theorem statement we make the assumption that $\dim N(L_0) = \dim N(L_0^*) = 1$ (i.e., the zero eigenvalue has geometric multiplicity 1). This condition is automatically satisfied in the case of models with one diffusing population. To see this, assume that there are q populations that have diffusion dynamics, and $p = n - q$ populations that do not. We write

$$\begin{aligned} \mathbf{u}(x) &= \begin{pmatrix} \mathbf{u}_1(x) \\ \mathbf{u}_2(x) \end{pmatrix}, \\ D &= \begin{pmatrix} D_0 & \\ & 0 \end{pmatrix}, \\ A(x) &= \begin{pmatrix} A_1(x) \\ A_2(x) \end{pmatrix}, \end{aligned}$$

where A_1 is a q -by- n and A_2 is a p -by- n matrix of the reaction rates. Then \mathbf{u} is in the null space of L_0 if

$$(8) \quad D_0 \partial_x^2 \mathbf{u}_1 + A_1(x) \mathbf{u} = 0,$$

$$(9) \quad A_2(x) \mathbf{u} = 0.$$

Since matrix $A(x)$ reflects conservation of the particles, the sum of each of its columns is 0. If we have $p = 1$ (one diffusing population), it is clear that the sum of the rows in matrix A_2 yields $-A_1$. Thus $A_2(x) \mathbf{u} = 0$ implies $A_1(x) \mathbf{u} = 0$, and therefore \mathbf{u}_1 satisfies the pure diffusion equation with Neumann boundary conditions: $D_0 \partial_x^2 \mathbf{u}_1 = 0$. This yields $\mathbf{u}_1 = 1$, and the vector \mathbf{u}_2 can then be found by solving the rank- p system for p unknowns in (8) with given \mathbf{u}_1 . Therefore, the dimension of the kernel is clearly one in this case.

For the case $q > 1$, the conservative nature of the rate matrix A also ensures that $(1, 1, \dots, 1)^T \in N(L_0^*)$; however, there is no guarantee that this is the only solution of $L_0^* \mathbf{v} = 0$ (see counterexample in Remark 3). This motivates our assumption that $\dim N(L_0^*) = 1$. We note, however, that models with two diffusing species and one nondiffusing population can also be shown to satisfy the theorem assumption.

Remark 3. An example of a system that does not satisfy the theorem assumption would consist of two decoupled copies of the 2-state system, each with an advection and a diffusion state. In this case, each individual system has an eigenvalue at 0 (with one corresponding eigenvector each). This means that the eigenvalue zero is no longer algebraically simple.

Remark 4. It is worth noting that the large-time form of $\mathbf{u}(\mathbf{r}, t)$ in Theorem 2.1 is similar to the asymptotic expansion developed formally for solutions of linear reaction-hyperbolic equations in [42] and rigorously proven in [15, 16], where the rates of the transition reactions are assumed to approach infinity. The result here generalizes these results for systems with diffusion in an arbitrary number of states and focuses on the large time limit for systems where no parameter assumptions are made.

2.4. Application to the 2-state model. We now discuss the implications of Theorem 2.1 for the 2-state system (2) with one moving and one diffusing particle population. Remark 2 of section 2.3 guarantees that the 2-state model satisfies the conditions of Theorem 2.1. We will show in section 2.6 that the effective velocity and diffusion of the particles under this model are given by the following expressions:

$$(10) \quad \begin{aligned} v_{\text{eff}} &= \frac{\langle \alpha \rangle}{\langle \alpha \rangle + \beta} v_0, \\ \sigma_{\text{eff}} &= \frac{\beta}{\langle \alpha \rangle + \beta} D_0 + \frac{\beta \langle \alpha \rangle}{(\beta + \langle \alpha \rangle)^3} v_0^2 + \frac{\beta}{(\beta + \langle \alpha \rangle)^2} v_0 \langle \alpha(x), w^0(x) \rangle, \end{aligned}$$

where $\langle \alpha \rangle = \int_0^1 \alpha(x) dx$, and $w^0(x)$ is the unique solution of

$$(11) \quad D_0 w_{xx}^0 = \frac{v_0}{\beta + \langle \alpha \rangle} (\langle \alpha \rangle - \alpha(x)), \quad w_x^0(0) = w_x^0(1) = 0.$$

Before discussing the implications of these results for transport, we briefly comment on the expressions we obtained above. First, when the filaments are equidistributed in the domain so that $\alpha(x) = \bar{\alpha}$ is a constant function, we have $\langle \alpha \rangle = \bar{\alpha}$, and therefore $w^0(x) = 0$, so that the effective velocity and diffusion constants in this simpler case are given by

$$(12) \quad v_{\text{eff}}^0 = \frac{\bar{\alpha}}{\bar{\alpha} + \beta} v_0, \quad \sigma_{\text{eff}}^0 = \frac{\beta}{\bar{\alpha} + \beta} D_0 + \frac{\beta \bar{\alpha}}{(\beta + \bar{\alpha})^3} v_0^2;$$

see also [10]. Next, we compare our results with those in [8], where the additional assumption $|\alpha| \ll \beta$ was used. In [8], the effective equation describing sum $c(\mathbf{r}, t) = \bar{p}(\mathbf{r}, t) + p_0(\mathbf{r}, t)$ of the particle populations for parallel filaments became

$$\frac{\partial c}{\partial t} = v_{\text{eff}} \frac{\partial c}{\partial y} + D(x, t) \nabla^2 c(\mathbf{r}, t) + Q_{yy}(x, t) \frac{\partial^2 c}{\partial y^2},$$

with effective velocity $v_{\text{eff}} = \frac{\alpha}{\beta} v_0$ and effective diffusion $D(x, t) + Q_{yy}(x, t) = (1 - \frac{\alpha}{\beta}) D_0 + \frac{\alpha}{\beta^2} v_0^2$ in the y -direction. While our results are very similar to these expressions (when using the hypothesis $|\alpha| \ll \beta$ that was used in [8]), it is worth noting that the expressions for the effective velocity and diffusion in [8] maintain the spatial dependence through the concentration of

signaling molecules $\alpha(x)$, whereas our large-time results depend only on the space-averaged quantity $\bar{\alpha}$. Note that the last term in our expression (10) for the effective diffusion is not captured by the analysis in [8]. The advantage of our method is that it allows derivation of complete expressions for effective velocity and diffusion under no assumptions on the density of the microtubules, the magnitude of the reaction rates, and the diffusion coefficient.

Next, we discuss the consequences of our results for transport. Comparing the expressions for the effective diffusion for general filament densities $\alpha(x)$ in (10) with those in (12) for constant α , we see that the expression for the effective diffusion in (10) contains the additional term $\frac{\beta}{(\beta + \langle \alpha \rangle)^2} v_0 \langle \alpha(x), w^0(x) \rangle$; it is this term that captures the density-dependence of diffusion. Our next result shows that diffusion is enhanced when the filament density is not constant.

Lemma 2.2. *For the 2-state advection-diffusion system (2) and any relevant parameters, the additional term in the effective diffusion expression is nonnegative:*

$$v = \frac{\beta}{(\beta + \langle \alpha \rangle)^2} v_0 \langle \alpha(x), w^0(x) \rangle \geq 0.$$

Proof. Noting that $\langle \alpha \rangle = \alpha$ in the case where filaments are assumed to be available throughout the domain,

$$\sigma_{\text{eff}} - \sigma_{\text{eff}}^0 = v.$$

To determine the sign of term v , we integrate (11) against w^0 :

$$(13) \quad \int_0^1 D_0 w_{xx}^0 w^0 dx = \frac{v_0}{\beta + \langle \alpha \rangle} \int_0^1 (\langle \alpha \rangle - \alpha(x)) w^0 dx.$$

Denoting $f = \frac{v_0}{\beta + \langle \alpha \rangle}$, we have

$$\int_0^1 \alpha(x) w^0(x) dx = (1/f) \left(f \langle \alpha \rangle \int_0^1 w^0(x) dx - \int_0^1 D_0 w_{xx}^0 w^0 dx \right).$$

Using that $\langle w^0(x) \rangle = 0$ and integration by parts combined with the Neumann boundary conditions in (11) yields

$$\int_0^1 \alpha(x) w^0 dx = (1/f) \int_0^1 D_0 (w_x^0)^2 dx \geq 0.$$

Therefore

$$v = \frac{\beta}{(\beta + \langle \alpha \rangle)^2} \frac{v_0}{f} \int_0^1 D_0 (w_x^0)^2 dx \geq 0,$$

so the additional term in (36) is nonnegative for all biologically relevant (positive) choices of the transition rates, diffusion coefficient, and velocity parameters. ■

We note that, as outlined in section 2.1, the function $\alpha(x)$ can be assumed to take the form of a step function, which clearly satisfies the requirement that $\inf\{|\alpha(x)|; x \in [0, 1], \alpha(x) \neq 0\} > 0$. Lemma 2.2 suggests that accounting for the microtubule geometry when modeling particle transport consistently increases the effective spread of the particles in the large time

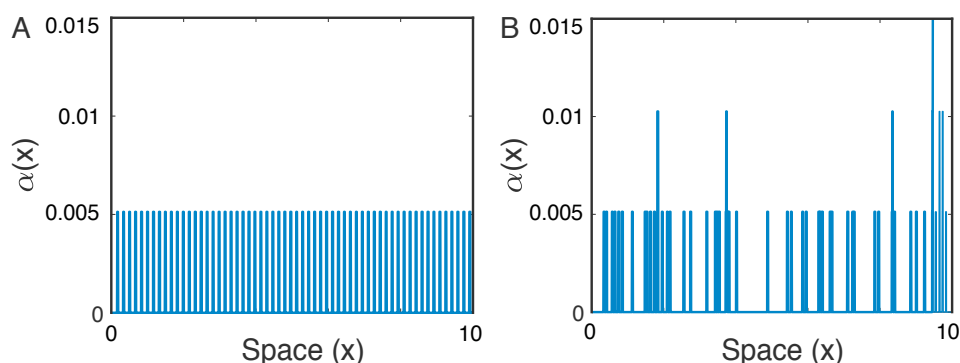


Figure 3. (A) Illustration of $\alpha(x)$ for a uniformly spaced microtubule structure. (B) Illustration of $\alpha(x)$ for a randomly spaced microtubule structure.

limit. In other words, we predict that the microtubule-dependent dynamics in equations (2) has a larger spatial variability (effective diffusion in (10)) than dynamics where the transition rates are assumed to be constant. To investigate how different arrangements of filaments may contribute differently to the effective diffusion, we consider functions $\alpha(x)$ that correspond to a uniform arrangement of microtubules (see Figure 3(A)) as well as a random arrangement of filaments (see Figure 3(B)). The disordered structure is of interest since previous modeling studies [18, 49] have found that such networks are more optimal in localization than perfectly aligned ones when considering the coupling of motor transport to fluid flow.

The contribution to the spread of particles is determined by integrating the second order equation (11),

$$D_0 w_{xx}^0 = \frac{v_0}{\beta + \langle \alpha \rangle} (\langle \alpha \rangle - \alpha(x)), \quad w_x^0(0) = w_x^0(1) = 0,$$

using a centered finite difference scheme. We consider this equation on a domain of 20–30 μm (10 μm visualized in Figure 3(A–B)) and assume a realistic microtubule diameter of 25 nm.

Figure 4 shows the percentage increase in the effective diffusion of particles for a set of parameters $(\bar{\alpha}, \beta, v_0, D)$ estimated from mRNA FRAP data in *Xenopus laevis* [10]. The choice of $\alpha(x)$ that reflects the uniform arrangement of microtubules in Figure 3(A) shows an increase of almost 10% (blue line) compared to the case where spatial microtubules are not modeled and $\alpha(x) = \alpha$ (constant). For $\alpha(x)$ corresponding to a random arrangement of microtubules, we consider 100 trials, with one sample distribution illustrated in Figure 3(B). In this case, the percentage increase varies for each random position trial (red dots), but the average increase reaches roughly 17% (yellow dotted line). While Figure 4 corresponds to a particular set of parameters, we confirmed the larger diffusivity in the random filament arrangement using additional parameters from data in other oocytes, as considered in [10].

2.5. Proof of Theorem 2.1.

Proof. Consider the ansatz

$$(14) \quad (u_1, \dots, u_n)^T = \bar{v}(x) e^{\lambda t + iky} \tilde{\mathbf{u}}_0,$$

where $\bar{v}(x)$ is a diagonal matrix whose j th diagonal entry is given by $v_j(x)$, and $\tilde{\mathbf{u}}_0$ is a vector

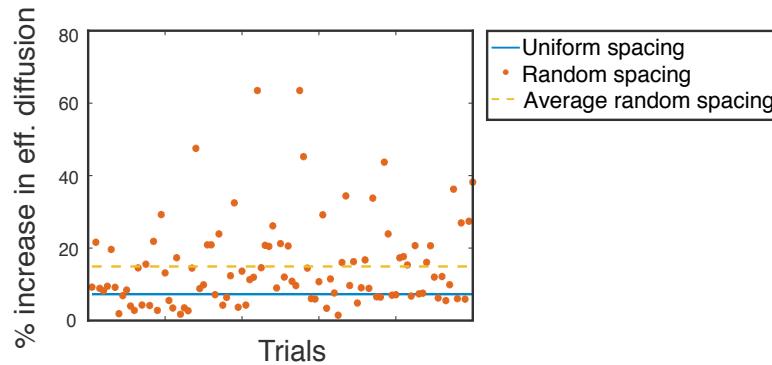


Figure 4. Increase in effective diffusion of particles when microtubules are arranged uniformly, as in Figure 3(A) (blue line), or randomly, as in Figure 3(B) (red dots for multiple trials and yellow dashed line for average).

of initial conditions. Plugging this into (3), we obtain

$$D\bar{v}_{xx}\tilde{\mathbf{u}}_0 + (A(x) + \nu C + \nu^2 D - \lambda I)\bar{v}(x)\tilde{\mathbf{u}}_0 = 0.$$

This suggests that we can incorporate vector $\tilde{\mathbf{u}}_0$ with matrix \bar{v} into a vector $\mathbf{v}(x)$ so that

$$(15) \quad D\mathbf{v}_{xx} + (A(x) + \nu C + \nu^2 D - \lambda I)\mathbf{v}(x) = 0.$$

We define the operator

$$L(\lambda, \nu) = D\partial_x^2 + A(x) + \nu C + \nu^2 D - \lambda I,$$

posed on $L^2([0, 1])$ with domain \mathcal{X} . Note that this operator is not necessarily self-adjoint: $L_0 = L(0, 0) = D\partial_x^2 + A(x)$ and $L_0^* = L^*(0, 0) = D\partial_x^2 + A^*(x)$. It follows from [46, Theorem 2.1] and the assumption that each entry of the reaction rate matrix $A(x)$ satisfies $\inf\{|a_{ij}(x)|; x \in [0, 1], a_{ij}(x) \neq 0\} > 0$ that the range of operator L is closed. The remaining assumptions in the theorem statement ensure that the null space and cokernel of operator L are one-dimensional and therefore that L is a Fredholm operator with index 0.

Since the null space of the Fredholm operator $L(0, 0)$ is finite-dimensional, we can apply the Lyapunov–Schmidt reduction theory to study the solutions of (15). For this construction, we take $\mathbf{v}(x) = a\mathbf{u}_0(x) + \mathbf{w}(x)$, where $\mathbf{w}(x)$ satisfies $\langle \boldsymbol{\psi}_0(x), \mathbf{w}(x) \rangle = 0$. We can now project the equation (rewritten below) on the range and kernel of the operator.

$$D\mathbf{v}_{xx} + (A(x) + \nu C + \nu^2 D - \lambda I)\mathbf{v}(x) = 0.$$

Projection on the range.

$$Lv - \frac{\langle Lv, \boldsymbol{\psi}_0 \rangle}{\langle \boldsymbol{\psi}_0, \mathbf{u}_0 \rangle} \mathbf{u}_0 = 0.$$

This gives

$$(16) \quad (D\partial_x^2 + A(x))\mathbf{w}(x) + (\nu C + \nu^2 D - \lambda I)(a\mathbf{u}_0 + \mathbf{w}) \\ - a \frac{\langle \boldsymbol{\psi}_0, (\nu C + \nu^2 D - \lambda I)\mathbf{u}_0 \rangle}{\langle \boldsymbol{\psi}_0, \mathbf{u}_0 \rangle} \mathbf{u}_0 - \frac{\langle \boldsymbol{\psi}_0, (\nu C + \nu^2 D - \lambda I)\mathbf{w} \rangle}{\langle \boldsymbol{\psi}_0, \mathbf{u}_0 \rangle} \mathbf{u}_0 = 0,$$

where we used that $L_0 \mathbf{u}_0 = 0$ and $L_0^* \psi_0 = 0$.

The third term above can be written as

$$a \frac{\langle \psi_0, (\nu C + \nu^2 D - \lambda I) \mathbf{u}_0 \rangle}{\langle \psi_0, \mathbf{u}_0 \rangle} \mathbf{u}_0 = -a\lambda \mathbf{u}_0 + a\nu(B_\nu \mathbf{u}_0) \mathbf{u}_0,$$

with B_ν taking \mathbf{x} to $\frac{\langle \psi_0, (C + \nu D) \mathbf{x} \rangle}{\langle \psi_0, \mathbf{u}_0 \rangle}$.

Similarly, the fourth term is

$$\frac{\langle \psi_0, (\nu C + \nu^2 D - \lambda I) \mathbf{w} \rangle}{\langle \psi_0, \mathbf{u}_0 \rangle} \mathbf{u}_0 = \nu(B_\nu \mathbf{w}) \mathbf{u}_0,$$

since $\langle \psi_0, \lambda \mathbf{w} \rangle = \lambda \langle \psi_0, \mathbf{w} \rangle = 0$.

Combining these, we obtain

$$(D\partial_x^2 + A(x) + \nu C + \nu^2 D - \lambda I - \nu \mathbf{u}_0 B_\nu) \mathbf{w}(x) + a(\nu C + \nu^2 D) \mathbf{u}_0 - a\lambda \mathbf{u}_0 + a\lambda \mathbf{u}_0 - a\nu(B_\nu \mathbf{u}_0) \mathbf{u}_0 = 0,$$

and therefore

$$(17) \quad (D\partial_x^2 + A(x) + \nu C + \nu^2 D - \lambda I - \nu \mathbf{u}_0 B_\nu) \mathbf{w}(x) + a(\nu C + \nu^2 D - \nu(B_\nu \mathbf{u}_0)) \mathbf{u}_0 = 0.$$

Projection on the kernel.

$$\langle \psi_0, L\nu \rangle = 0.$$

This gives

$$\langle \psi_0, (D\partial_x^2 + A(x) + \nu C + \nu^2 D - \lambda I)(a\mathbf{u}_0(x) + \mathbf{w}(x)) \rangle = 0.$$

Using $L_0 \mathbf{u}_0 = 0$, $\langle \psi_0(x), \mathbf{w}(x) \rangle = 0$, and $L_0^* \psi_0 = 0$,

$$\langle \psi_0, (\nu C + \nu^2 D - \lambda I)a\mathbf{u}_0(x) + (\nu C + \nu^2 D)\mathbf{w}(x) \rangle = 0.$$

Therefore

$$(18) \quad \begin{aligned} \lambda &= \frac{\langle \psi_0, (\nu C + \nu^2 D)(a\mathbf{u}_0(x) + \mathbf{w}(x)) \rangle}{a\langle \psi_0, \mathbf{u}_0 \rangle} \\ &= \nu \frac{\langle \psi_0, C\mathbf{u}_0 \rangle}{\langle \psi_0, \mathbf{u}_0 \rangle} + \nu^2 \frac{\langle \psi_0, D\mathbf{u}_0 \rangle}{\langle \psi_0, \mathbf{u}_0 \rangle} + \nu \frac{\langle \psi_0, (C + \nu D)\mathbf{w} \rangle}{a\langle \psi_0, \mathbf{u}_0 \rangle}, \end{aligned}$$

where \mathbf{w} satisfies (17).

Note that (17) can be expressed as $h(\nu, \mathbf{w}(x)) = 0$, where $h(0, \mathbf{u}_0) = 0$ and $\lambda(0) = 0$ given (18). Since $\frac{\partial h}{\partial \mathbf{w}}|_{(0, \mathbf{u}_0)} = D\partial_x^2 + A(x)$ with homogeneous Neumann boundary conditions in the diffusing states, we conclude that $\mathbf{w}(x) = g(\nu, x)$ for each x . Let

$$(19) \quad \mathbf{w}(x) = \nu \mathbf{w}_0(x) + \nu^2 \mathbf{w}_1(x) + \mathcal{O}(\nu^3).$$

It follows that (18) becomes

$$(20) \quad \lambda = \nu \frac{\langle \psi_0, C\mathbf{u}_0 \rangle}{\langle \psi_0, \mathbf{u}_0 \rangle} + \nu^2 \frac{\langle \psi_0, D\mathbf{u}_0 \rangle}{\langle \psi_0, \mathbf{u}_0 \rangle} + \nu^2 \frac{\langle \psi_0, C\mathbf{w}_0(x) \rangle}{a\langle \psi_0, \mathbf{u}_0 \rangle} + \mathcal{O}(\nu^3).$$

We therefore need to determine $\mathbf{w}_0(x)$. Plugging the expansion of \mathbf{w} in the projection into the range in (17), we obtain

$$(21) \quad \left(D\partial_x^2 + A(x) + \nu C + \nu^2 D - \nu \frac{\langle \psi_0, C\mathbf{u}_0 \rangle}{\langle \psi_0, \mathbf{u}_0 \rangle} I + \mathcal{O}(\nu^2) I - \nu \mathbf{u}_0 B_\nu \right) (\nu \mathbf{w}_0(x) + \nu^2 \mathbf{w}_1(x) + \mathcal{O}(\nu^3)) + a(\nu C + \nu^2 D - \nu(B_\nu \mathbf{u}_0)) \mathbf{u}_0 = 0.$$

By collecting powers of ν in (21), we have for $\mathcal{O}(\nu)$

$$(22) \quad (D\partial_x^2 + A(x))\mathbf{w}_0(x) + aC\mathbf{u}_0(x) - a \frac{\langle \psi_0, C\mathbf{u}_0 \rangle}{\langle \psi_0, \mathbf{u}_0 \rangle} \mathbf{u}_0(x) = 0.$$

Writing $\lambda = a_1\nu + a_2\nu^2 + \mathcal{O}(\nu^3)$ yields

$$(23) \quad a_1 = \frac{\langle \psi_0, C\mathbf{u}_0 \rangle}{\langle \psi_0, \mathbf{u}_0 \rangle},$$

$$(24) \quad a_2 = \frac{\langle \psi_0, D\mathbf{u}_0 \rangle}{\langle \psi_0, \mathbf{u}_0 \rangle} + \frac{\langle \psi_0, C\mathbf{w}_0(x) \rangle}{a\langle \psi_0, \mathbf{u}_0 \rangle},$$

where $\mathbf{w}_0 \in \mathcal{X}$ satisfies (22).

We now return with this expansion to the ansatz in (14). We are particularly interested in recovering the concentration of particles in each state for large time given these expansions. Using the inverse Fourier transform gives

$$(25) \quad \begin{aligned} \mathbf{u}(\mathbf{r}, t) &\approx \frac{1}{2\pi} \int_{-\delta}^{\delta} (a\mathbf{u}_0(x) + \mathbf{w}(x)) e^{\lambda t + iky} dk \\ &= \frac{1}{2\pi} \int_{-\delta}^{\delta} (a\mathbf{u}_0(x) + \mathbf{w}(x)) e^{ik(y+a_1t) - a_2k^2t} e^{\sum_{j=3}^{\infty} a_j (ik)^j t} dk, \end{aligned}$$

with δ small. Making the change of variable $\tilde{k} = kt^{1/2}$ and $\tilde{y} = y + a_1t$ yields

$$(26) \quad \begin{aligned} \mathbf{u}(\mathbf{r}, t) &\approx \frac{1}{2\pi\sqrt{t}} \int_{-\delta\sqrt{t}}^{\delta\sqrt{t}} (a\mathbf{u}_0(x) + \mathbf{w}(x)) e^{i\tilde{k}\frac{\tilde{y}}{t^{1/2}} - \frac{a_2}{2}\tilde{k}^2} e^{\sum_{j=3}^{\infty} a_j \frac{(i\tilde{k})^j}{t^{j/2-1}}} d\tilde{k} \\ &= \frac{1}{2\pi\sqrt{t}} \int_{-\delta\sqrt{t}}^{\delta\sqrt{t}} \left(a\mathbf{u}_0(x) + i\frac{\tilde{k}}{t^{1/2}} \mathbf{w}_0(x) - \frac{\tilde{k}^2}{t} \mathbf{w}_1(x) + \sum_{j=1}^{\infty} \frac{(i\tilde{k})^j}{t^{j/2}} \mathbf{w}_{j-1}(x) \right) \\ &\quad \times \exp\left(i\tilde{k}\frac{\tilde{y}}{t^{1/2}} - \frac{a_2}{2}\tilde{k}^2\right) \exp\left(\sum_{j=3}^{\infty} a_j \frac{(i\tilde{k})^j}{t^{j/2-1}}\right) d\tilde{k}. \end{aligned}$$

Since we are interested in long-term asymptotic behavior at $t \rightarrow \infty$, we note that the dominant term in the expression in the parentheses is $a\mathbf{u}_0(x)$ and that the last exponential term in (27) converges to 1. Therefore

$$(27) \quad \mathbf{u}(\mathbf{r}, t) \approx \frac{1}{2\pi\sqrt{t}} a\mathbf{u}_0(x) \int_{-\infty}^{\infty} e^{i\tilde{k}\frac{\tilde{y}}{t^{1/2}} - \frac{a_2}{2}\tilde{k}^2} d\tilde{k} = \frac{a}{\sqrt{2\pi a_2 t}} e^{\frac{(y+a_1t)^2}{2a_2t}} \mathbf{u}_0(x).$$

The Gaussian form of the asymptotic solution for large time provides the effective velocity and effective diffusion of the particles, given by a_1 and a_2 , respectively, in (23) and (24). ■

2.6. Proof of the 2-state model results.

Setup for the 2-state system. In the 2-state model, the setup for (15) is as follows:

$$C = \begin{pmatrix} v_0 & 0 \\ 0 & 0 \end{pmatrix}, \quad D = \begin{pmatrix} 0 & 0 \\ 0 & D_0 \end{pmatrix}, \quad A(x) = \begin{pmatrix} -\beta & \alpha(x) \\ \beta & -\alpha(x) \end{pmatrix}.$$

We assume that $\beta > 0$ and that $\alpha(x) \in L^2([0, 1])$ satisfies $\inf\{|\alpha(x)|; x \in [0, 1], \alpha(x) \neq 0\} > 0$. Solving $L(0, 0) = 0$ is equivalent to solving

$$(28) \quad \begin{aligned} -\beta v_1(x) + \alpha(x)v_2(x) &= 0, \\ D_0 \partial_x^2(v_2) + \beta v_1(x) - \alpha(x)v_2(x) &= 0, \end{aligned}$$

so that $D_0(v_2)_{xx} = 0$, and with the homogeneous Neumann boundary conditions for v_2 , we find that $v_2 = 1$ (constant). Then $v_1 = \alpha(x)/\beta$, yielding

$$N(L(0, 0)) = (\alpha(x)/\beta, 1)^T.$$

Similarly for $N(L^*(0, 0))$, we solve

$$(29) \quad \begin{aligned} -\beta(v_1(x) - v_2(x)) &= 0, \\ D \partial_x^2(v_2) + \alpha(x)(v_2(x) - v_1(x)) &= 0, \end{aligned}$$

which yields $v_1 = v_2 = 1$. Thus

$$N(L^*(0, 0)) = (1, 1)^T,$$

so that both null spaces are finite and have dimension 1. The assumption in the theorem is therefore satisfied.

Results for the 2-state system. We now write the results in (23) and (24) in the context of the 2-state model. In this case we have

$$\begin{aligned} \boldsymbol{\psi}_0 &= (1, 1)^T, \\ \boldsymbol{u}_0 &= (\alpha(x)/\beta, 1)^T, \end{aligned}$$

and $\langle \boldsymbol{\psi}_0, \boldsymbol{u}_0 \rangle = \langle 1, \alpha(x) \rangle / \beta + 1 = \frac{\beta + \langle 1, \alpha(x) \rangle}{\beta}$.

The fact that $\boldsymbol{w} \in N(L_0^*)^\perp$ means that

$$\int_0^1 w_1(x) + w_2(x) dx = 0$$

for $\boldsymbol{w}(x) = (w_1(x), w_2(x))^T$. This implies that $\int_0^1 w_2(x) = -\int_0^1 w_1(x)$.

Writing $\lambda = a_1\nu + a_2\nu^2 + \mathcal{O}(\nu^3)$ and using (23), we have

$$(30) \quad a_1 = v_{\text{eff}} = \frac{\langle \boldsymbol{\psi}_0, C\boldsymbol{u}_0 \rangle}{\langle \boldsymbol{\psi}_0, \boldsymbol{u}_0 \rangle} = \frac{v_0 \langle 1, \alpha(x) \rangle / \beta}{\frac{\langle 1, \alpha(x) \rangle + \beta}{\beta}} = \frac{\langle 1, \alpha(x) \rangle}{\langle 1, \alpha(x) \rangle + \beta} v_0.$$

Similarly, the first term in a_2 is

$$(31) \quad \frac{\langle \psi_0, D\mathbf{u}_0 \rangle}{\langle \psi_0, \mathbf{u}_0 \rangle} = \frac{D_0}{\frac{\langle 1, \alpha(x) \rangle + \beta}{\beta}} = \frac{\beta}{\langle 1, \alpha(x) \rangle + \beta} D_0.$$

We now need to evaluate the second term in a_2 , namely,

$$\frac{\langle \psi_0, C\mathbf{w}_0(x) \rangle}{\langle \psi_0, \mathbf{u}_0 \rangle} = \frac{\beta}{\beta + \langle 1, \alpha(x) \rangle} v_0 \langle 1, w_1(x) \rangle,$$

where $\mathbf{w}_0(x) = (w_1(x), w_2(x))^T$. Recall that \mathbf{w}_0 satisfies (22):

$$(D\partial_x^2 + A(x))\mathbf{w}_0(x) + aC\mathbf{u}_0(x) - a \frac{\langle \psi_0, C\mathbf{u}_0 \rangle}{\langle \psi_0, \mathbf{u}_0 \rangle} \mathbf{u}_0(x) = 0.$$

Therefore

$$\begin{pmatrix} 0 & 0 \\ 0 & D_0 \end{pmatrix} \begin{pmatrix} (w_1)_{xx} \\ (w_2)_{xx} \end{pmatrix} + \begin{pmatrix} -\beta & \alpha(x) \\ \beta & -\alpha(x) \end{pmatrix} \begin{pmatrix} w_1 \\ w_2 \end{pmatrix} + \begin{pmatrix} v_0\alpha(x)/\beta \\ 0 \end{pmatrix} - \frac{\langle 1, \alpha(x) \rangle}{\langle 1, \alpha(x) \rangle + \beta} v_0 \begin{pmatrix} \alpha(x)/\beta \\ 1 \end{pmatrix} = 0.$$

This is equivalent to solving the system

$$\begin{aligned} -\beta w_1 + \alpha(x)w_2 + v_0 \frac{\alpha(x)}{\beta + \langle 1, \alpha(x) \rangle} &= 0, \\ D_0(w_2)_{xx} + \beta w_1 - \alpha(x)w_2 - v_0 \frac{\langle 1, \alpha(x) \rangle}{\beta + \langle 1, \alpha(x) \rangle} &= 0, \end{aligned}$$

which then yields

$$(32) \quad \begin{aligned} D_0(w_2)_{xx} &= \frac{v_0}{\beta + \langle 1, \alpha(x) \rangle} (\langle 1, \alpha(x) \rangle - \alpha(x)), \\ w_1(x) &= \frac{v_0\alpha(x)}{\beta(\beta + \langle 1, \alpha(x) \rangle)} + \frac{\alpha(x)}{\beta} w_2(x). \end{aligned}$$

Therefore

$$\begin{aligned} \frac{\langle \psi_0, C\mathbf{w}_0(x) \rangle}{\langle \psi_0, \mathbf{u}_0 \rangle} &= \frac{\beta}{\beta + \langle 1, \alpha(x) \rangle} v_0 \langle 1, w_1(x) \rangle \\ &= \frac{\langle 1, \alpha(x) \rangle}{(\beta + \langle 1, \alpha(x) \rangle)^2} v_0^2 + \frac{1}{(\beta + \langle 1, \alpha(x) \rangle)} v_0 \langle \alpha(x), w_2(x) \rangle, \end{aligned}$$

where w_2 satisfies (32).

Noting that the right-hand-side (RHS) of (32) satisfies $\langle RHS \rangle = \int_0^1 RHS = 0$, we write $w_2 = d + w_2^0$ with arbitrary $d \in \mathbb{R}$ and $\langle w_2^0 \rangle = 0$. w_2^0 then satisfies (32) as well. This gives

$$\begin{aligned} w_1 &= \frac{v_0\alpha(x)}{\beta(\beta + \langle 1, \alpha(x) \rangle)} + \frac{\alpha(x)}{\beta} d + \frac{\alpha(x)}{\beta} w_2^0(x), \\ \langle w_1 \rangle + \langle w_2 \rangle &= \frac{v_0\alpha(x)}{\beta(\beta + \langle 1, \alpha(x) \rangle)} + \frac{\alpha(x)}{\beta} d + \frac{\alpha(x)}{\beta} w_2^0(x) + d = 0. \end{aligned}$$

From this, we find

$$d = -\frac{1}{\langle \alpha \rangle + \beta} \left(\frac{\langle \alpha \rangle}{\langle \alpha \rangle + \beta} v_0 + \langle \alpha w_2^0 \rangle \right),$$

and the expression for w_1 :

$$(33) \quad w_1 = \frac{\langle \alpha \rangle}{(\langle \alpha \rangle + \beta)^2} v_0 - \frac{\langle \alpha \rangle}{\beta(\langle \alpha \rangle + \beta)} \langle \alpha w_2^0 \rangle + \frac{\alpha}{\beta} w_2^0.$$

Then the second term in a_2 becomes

$$(34) \quad \begin{aligned} \frac{\langle \psi_0, C w_0(x) \rangle}{\langle \psi_0, u_0 \rangle} &= \frac{\beta}{\beta + \langle 1, \alpha(x) \rangle} v_0 \langle 1, w_1(x) \rangle \\ &= \frac{\beta \langle \alpha(x) \rangle}{(\beta + \langle 1, \alpha(x) \rangle)^3} v_0^2 + \frac{1}{(\beta + \langle 1, \alpha(x) \rangle)} v_0 \langle \alpha(x), w_2^0(x) \rangle \left(-\frac{\langle \alpha \rangle}{(\beta + \langle 1, \alpha(x) \rangle)} + 1 \right) \\ &= \frac{\beta \langle \alpha(x) \rangle}{(\beta + \langle 1, \alpha(x) \rangle)^3} v_0^2 + \frac{\beta}{(\beta + \langle 1, \alpha(x) \rangle)^2} v_0 \langle \alpha(x), w_2^0(x) \rangle. \end{aligned}$$

Collecting all the derived terms, we conclude that

$$(35) \quad a_1 = v_{\text{eff}} = \frac{\langle 1, \alpha(x) \rangle}{\langle 1, \alpha(x) \rangle + \beta} v_0,$$

$$(36) \quad a_2 = \sigma_{\text{eff}} = \frac{\beta}{\langle 1, \alpha(x) \rangle + \beta} D_0 + \frac{\beta \langle 1, \alpha(x) \rangle}{(\beta + \langle 1, \alpha(x) \rangle)^3} v_0^2 + \frac{\beta}{(\beta + \langle 1, \alpha(x) \rangle)^2} v_0 \langle \alpha(x), w_2^0(x) \rangle$$

with

$$(37) \quad D_0(w_2^0)_{xx} = \frac{v_0}{\beta + \langle 1, \alpha(x) \rangle} (\langle 1, \alpha(x) \rangle - \alpha(x)), \quad (w_2^0)_x(0) = (w_2^0)_x(1) = 0.$$

As discussed in section 2.4, this calculation agrees with the results of the quasi-steady-state analysis in [8] given their assumption $\alpha(x) \ll \beta$ (which implies $\frac{\beta}{\beta + \alpha(x)} \approx 1$).

3. Random planar microtubule networks and anchoring of mRNA. Our analytical approach applies to determining the large time mobility behavior of biological particles under the assumption of a parallel array of microtubular filaments. However, *Xenopus laevis* oocytes display microtubules that are randomly oriented in the cytoplasm, with a bias towards a radially outward orientation (see [17, Figure S3]). Therefore, we construct microtubule structures $\rho(\mathbf{r}, \theta)$ that reflect this outward orientation by adapting the approach proposed in [48] (see Figure 5(A)). Since the large-time analysis is more challenging under the assumption of radially outward microtubules, we use multiple model microtubule structures combined with a more realistic model and a numerical approach similar to [48] to investigate the mRNA spatial distribution at different times during localization.

3.1. Four-state transport model and choice of microtubule networks. In [10], we showed that accounting for bidirectional transport of mRNA using a more complex 4-state model leads to parameter estimation results that agree well with the mRNA localization data in *Xenopus laevis* oocytes [17]. Here we extend the 4-state model in [10] to incorporate the underlying

microtubule networks on which active transport of mRNA occurs. In equations (38), u^+ corresponds to a population of particles carried by one type of motor protein down to the vegetal cortex, u^- corresponds to a population transported by other motor proteins up to the nucleus, v is a population freely diffusing in the cytoplasm with diffusion coefficient d , and w corresponds to a population of mRNA paused on the microtubules. As before, these variables refer to the concentrations of particles in each of these states. The switching of the mRNA between these four different dynamical states occurs through binding and unbinding reactions as follows:

$$\begin{aligned}
 (38a) \quad & v_t = d\Delta v - \beta_+ v + \gamma_+ u^+ - \beta_- v + \gamma_- u^-, \\
 (38b) \quad & u_t^+ = \nabla(c_+ \mathbf{v}_m u^+) + \beta_+ v - \gamma_+ u^+ + \alpha_+ w - \delta_+ u^+, \\
 (38c) \quad & u_t^- = -\nabla(c_- \mathbf{v}_m u^-) + \beta_- v - \gamma_- u^- + \alpha_- w - \delta_- u^-, \\
 (38d) \quad & w_t = \delta_+ u^+ + \delta_- u^- - \alpha_+ w - \alpha_- w,
 \end{aligned}$$

where \mathbf{v}_m is a velocity field as in [10] derived from the assumed cytoskeletal network that we describe in section 3.2. The transition rates between the four different states are illustrated in [48, Figure 3B]. We note that these equations extend the 2-state model in [48], but do not account for cytoplasmic flow driven by kinesin motor transport. In *Drosophila* oocytes, the mRNAs are synthesized in the attached nurse cells and transported into the oocyte, so cytoplasmic flows may be important in the mobility of RNA [58]. By contrast, in *Xenopus*, oocyte mRNAs are synthesized in the oocyte nucleus, and thus we do not consider flows in our simulations of mRNA localization. It is also worth noting that [48] concludes that the cytoplasmic flows do not play a key role in the localization process.

Given the randomness in microtubule orientations in many biological systems [18], our findings in section 2.4 motivate the study of particle dynamics using realistic geometries of the cytoskeleton informed from experimental data. To better understand mRNA localization mechanisms in *Xenopus* oocytes, we therefore consider accurate filament orientations inspired from microtubule experiments in [17, 19]. In particular, we first generate model microtubule structures by adapting the algorithm in [48] to reflect a two-dimensional geometry and the assumptions needed for *Xenopus laevis* oocytes. To create the microtubule network, a random cytoplasmic location (in the circular annulus excluding the nucleus) is chosen as an initiation point for each microtubule. For the microtubule lengths, we consider an exponential distribution of filament lengths and assume that the mean microtubule length is $9 \mu\text{m}$, as informed by [20, 21, 38, 45]. Both our results and the findings in [48] are not changed by considering this simpler exponential distribution of microtubule lengths instead of a Gamma distribution that has been proposed to describe the catastrophe lengths of microtubules observed experimentally [21].

As in [48], we model each microtubule as a sequence of straight polymer segments with variable orientations. The direction of the first segment is generated in an outward radial direction or drawn randomly and accepted only if the orientation is pointing inside the allowed geometry [48] (oocyte annulus in our case). For the subsequent segments, we draw directions from the von Mises distribution on a circle with a given likelihood that the next generated segment has a similar orientation to the previous one [48]. For most simulations, the bias for a radially outward orientation of microtubules in *Xenopus* oocytes [19] leads to our modeling

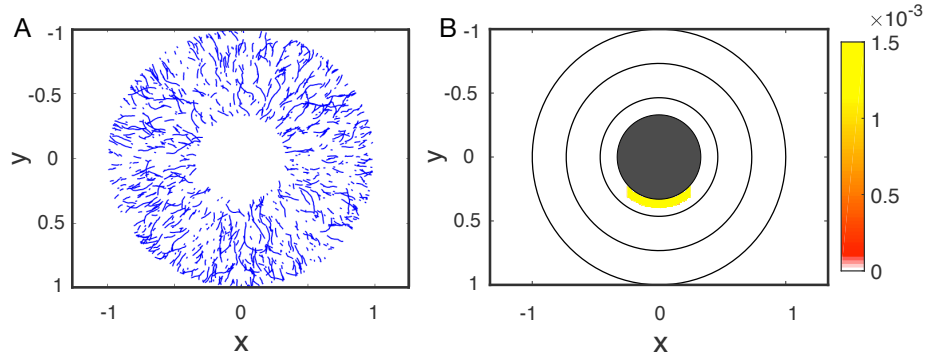


Figure 5. (A) Sample microtubule structure with 1000 filaments. (B) Initial mRNA particle distribution assuming that the mRNA initially accumulates next to the nucleus. Color bar for the constructed color map is included: yellow corresponds to a high density of mRNA, and increasingly red shades denote smaller concentrations of mRNA; white regions have no mRNA traces.

assumption that half of the microtubules start with random orientations and half start with radially outward orientations in the first segment.

Simulations of localization discussed in the next sections are run with 50000–60000 filaments for numerical stability, with Figure 5(A) showing a sample microtubule structure with 1000 filaments for ease of visualization. While it is challenging to quantify the differences between these model structures and images of the microtubule cytoskeleton as in [4, 19], these structures compare well visually with the observed experimental structures. It is worth noting that the microtubule filaments are dynamic and undergo catastrophes on the timescale of localization, with mean lifetimes of roughly 5 minutes on average [21]. As a result, we generate multiple such structures and draw from them at random to set a distinct background microtubule structure at each hour in the simulation of the partial differential equation models (38) considered (more frequent changes do not impact results but increase the computational time).

3.2. Numerical simulations of transport dynamics. In this section we discuss numerical and data analysis methods that will be used in section 3.3 below to develop simulations of mRNA localization in *Xenopus* oocytes and to compare results to experimental images.

We consider a two-dimensional domain corresponding to a circular oocyte of radius $150 \mu\text{m}$ (the average radius for oocytes in stage II of oogenesis [17]) and nucleus of radius $50 \mu\text{m}$. In our simulations, we nondimensionalize lengths so that we consider radius $R = 1$, $x \in [-1, 1]$, and $y \in [-1, 1]$. The grid size in our simulations of localization is a square of side $1.5 \mu\text{m}$. To ensure that we can simulate transport along microtubules for the advection term in the simulations, we find that we need roughly 9 microtubule segments on average per square grid. Assuming a microtubule diameter of 25 nm , a uniform distribution of microtubules would correspond in our simulations to an average distance of $0.14 \mu\text{m}$ between microtubules. While there are no references for microtubule spacing in live egg cells, this value is on a similar order of magnitude to distances between microtubule bundles in axons and dendrites ($0.02\text{--}0.065 \mu\text{m}$) [27].

In addition, we follow the approach in [48] to calculate the velocity field \mathbf{v}_m (see (38)) where active transport by molecular motor proteins can occur. For this, we calculate the

midpoint of each microtubule segment, and sum vectorially the orientations of all segments whose midpoints are located in the same grid area [48]. After normalizing, this yields a local motor-velocity vector field representing the direction along which mRNA molecules can be actively transported by kinesin or dynein motor proteins.

The dynamics of the mRNA is then simulated using the 4-state model in equations (38). The partial differential equations are solved using a finite-volume discretization on staggered grids with no flux boundary conditions [48,54]. Our implementation of the numerical methods extends the algorithm in [48] to account for two active transport states as well as an additional paused state as modeled in equations (38). In addition to considering bidirectional transport in the 4-state model, our simulations use realistic spatially dependent parameters that we previously estimated from FRAP data in [10]. We note that in that study we carried out parameter estimation in 3 annular regions where FRAP experiments are performed in the oocyte cytoplasm [10,17]. Here we assume that Region 1 extends $20\text{ }\mu\text{m}$ from the nucleus into the cytoplasm, and Region 3 extends $40\text{ }\mu\text{m}$ from the vegetal cortex into the cytoplasm (see Figure 5(B)). We use distinct parameters for each region as estimated in [10] (d , c_+ , c_- , α_+ , α_- , δ_+ , δ_-) and set the microtubule binding/unbinding rates (β_+ , β_- , γ_+ , γ_-) constant as justified in [10]. In our simulations, we set a smooth transition (modeled by a tanh function) over a small spatial radius for parameters that vary in adjacent annular regions. In addition, we set the velocity of the moving population to 0 at the cortex boundary and allow this speed to decrease from its estimated value in the cytoplasm to 0 in a smooth way as well.

The initial conditions for equations (38) are set to model the early initial accumulation of mRNA in the perinuclear cup region (under the nucleus) in stage II-III *Xenopus* oocytes [17]. We consider a uniform initial condition over a region comparable to experimental observations as illustrated in Figure 5(B). This figure also provides the MATLAB color map created to visualize the results of our simulations and to compare with [17, Figures 1C, 3D, and S2, A–C].

To compare the results of our numerical simulations with experiments, we consider snapshots of the mRNA distribution at different times throughout localization, as provided in [17], as well as the time evolution of the mRNA distribution, as provided in the accompanying video (M118608.01.avi [local/web 1.54MB]). To extract additional spatial information from the experimental images, cytoplasmic RNA localization in experimental images is also quantified using a custom macro developed for the Fiji distribution of the image processing program ImageJ (version 1.51k; [43,44]). The macro, which is available at [29], measures the fluorescence intensity in two-dimensional concentric rings (bins) within the oocyte. Based on user-defined input of oocyte and nuclear diameter, the program creates five equally spaced concentric rings (bins) starting at the oocyte periphery and ending at the nuclear periphery. To avoid signal from background and autofluorescence, a threshold is set to consider only pixels within 50% of the maximum observed pixel intensity. The amount of fluorescence is then measured and recorded for each annulus region that forms between consecutive rings.

3.3. Insights into mRNA localization and anchoring at the cell cortex.

The proposed model for mRNA transport on microtubules reproduces observed spatial scales of localization. Figure 6 illustrates the distribution of total mRNA 10 hours (left) and 24 hours (right) into localization. The top panel corresponds to simulations with model microtubule

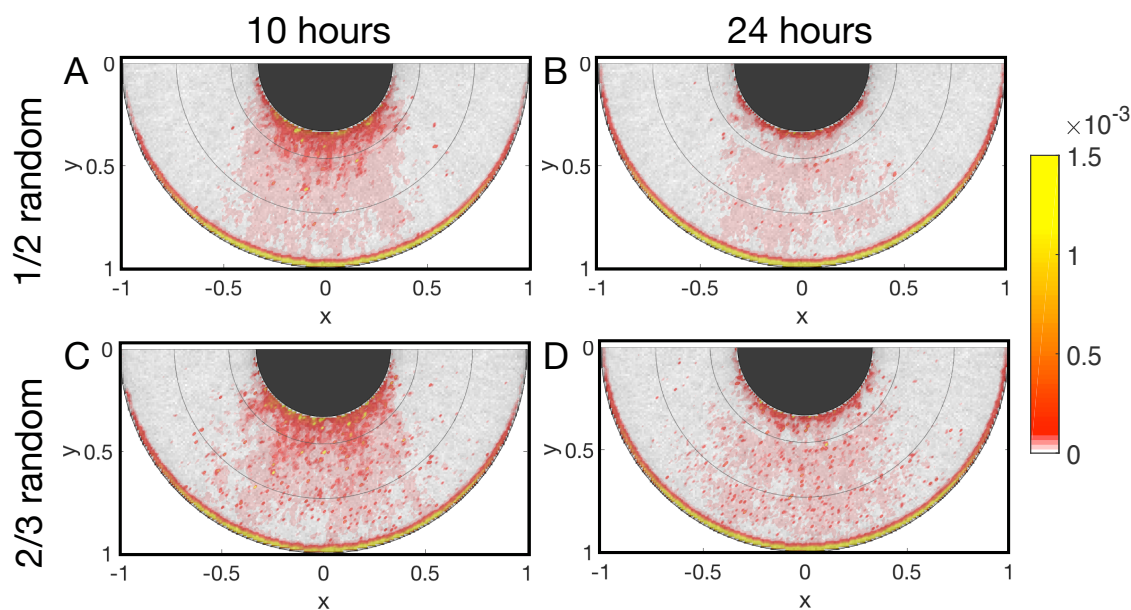


Figure 6. Predicted mRNA localization distributions 10 (A, C) and 24 (B, D) hours into localization, with transport restricted to microtubule structures (gray background) as in Figure 5(A) (see also the accompanying video file M118608_01.avi [local/web 1.54MB]). The concentric circles drawn in black divide three regions of the vegetal cytoplasm where FRAP experiments have been performed [17]; rate and velocity parameters are constant within each region but differ across regions [10]. (A, B) The label 1/2 random corresponds to starting random orientations in half of the model microtubules. (C, D) The label 2/3 random corresponds to two-thirds of the filaments initialized with random orientations. The color bar from Figure 5 is included.

structures where half of the filaments are initialized with random orientations and half with a radial outward direction. The bottom panel corresponds to simulations where two-thirds of the filaments start out with random orientations, leading to a significantly more spread out distribution of mRNA throughout the process. We note that the simulation is run on a full circular oocyte, but the dynamics is confined to the vegetal half cytoplasm (as shown) due to the initial accumulation of the particles. In addition, the gray background corresponds to the averaged density of microtubules at each location. This approach allows for comparison to imaging results obtained through injection of fluorescently labeled RNA in *Xenopus* oocytes [17]. The top panel of Figure 6 predicts that the particles are largely confined to a wedge region in the lower cytoplasm, which compares well with the spatial distribution of mRNA in [17, Figures 1C, 3D, and S2, A–C]; see also the accompanying video (M118608_01.avi [local/web 1.54MB]) for an hour-by-hour predicted evolution of the mRNA distribution.

Anchoring a moving population of mRNA particles may be most efficient in achieving faster localization. An alternative way to quantify the amount of mRNA localized at the vegetal cortex is visualized in Figure 7(A). There, we plot the time evolution of the fraction of mRNA located within 10% of the cortex, as predicted by our simulations. We note that the fraction of localized mRNA reaches roughly 80% in 24 hours of localization, and only slightly increases at the end of 48 hours (results not shown). Since complete localization of mRNA is crucial at this stage of egg cell development and normally occurs within 1–2 days, our results suggest

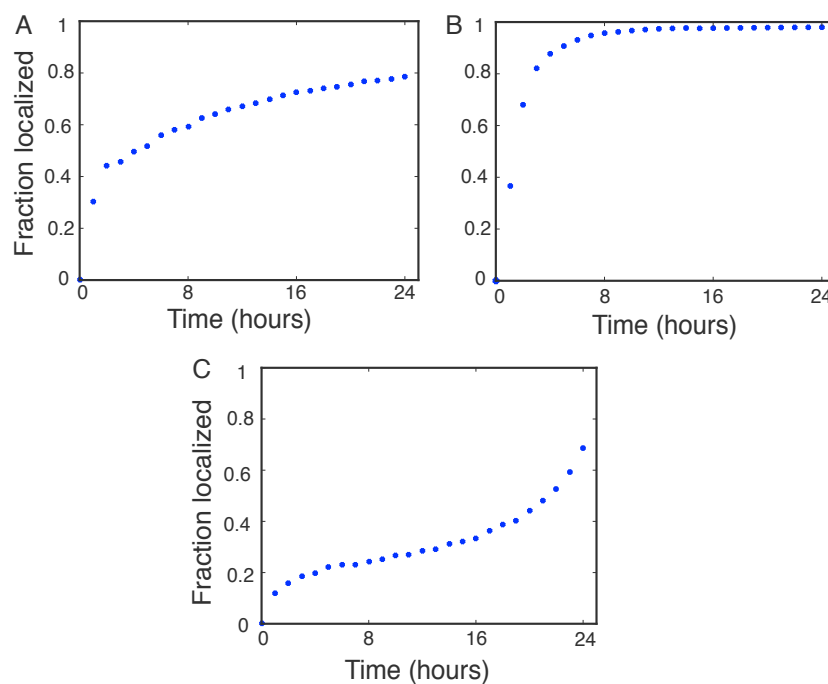


Figure 7. Predicted fraction of mRNA within 10% of the cortex throughout 24 hours of localization for a sample oocyte with no anchoring (A); with anchoring of the transport down state near the vegetal cortex (B); and with time-dependent anchoring near the vegetal cortex as described in the text (C). The spatial distribution of the simulated particles at 10 and 24 hours into localization corresponding to (A) is illustrated in Figure 6(A, B).

that a potential anchoring mechanism at the cortex may contribute to the observed timescale of healthy localization and development in *Xenopus* oocytes.

While previous studies agree that Vg1 mRNA is anchored at the cell cortex, the mechanisms of this process are not known. Cytoskeleton-dependent RNA anchoring has been suggested in other developmental systems. In *Drosophila*, both actin and microtubules have been implicated in anchoring RNA in oocytes and embryos, respectively [2, 12]. Likewise, pharmacological disruption of actin microfilaments [31, 55] in *Xenopus* oocytes causes the release of anchored Vg1 mRNA from the cortex. Evidence for microtubule-mediated anchoring in *Xenopus* oocytes has been inconclusive [1, 31], but other cytoskeletal elements, such as cytokeratins, have been implicated [1, 33]. Cytoskeleton interacting proteins have also shown a critical role in RNA anchoring in the *Drosophila* oocytes. Such factors include actin-associated proteins [2], endocytic pathway components [47], locally synthesized maternal determinants [53], and even the motor protein dynein [11, 12]. Although no anchoring protein has been identified in *Xenopus*, depletion of other localized RNAs releases anchored Vg1 mRNA, suggesting a potential RNA-dependent RNA anchoring mechanism [24, 30, 32]. Despite the limited experimental insight into the anchoring mechanisms, our model allows us to investigate the importance of this process by changing the transition rates between states in an anchoring region (assumed to be 5% from the cortex in our simulations).

In the 4-state model (38) that yields the spatial localization in Figures 6(A, B), we can

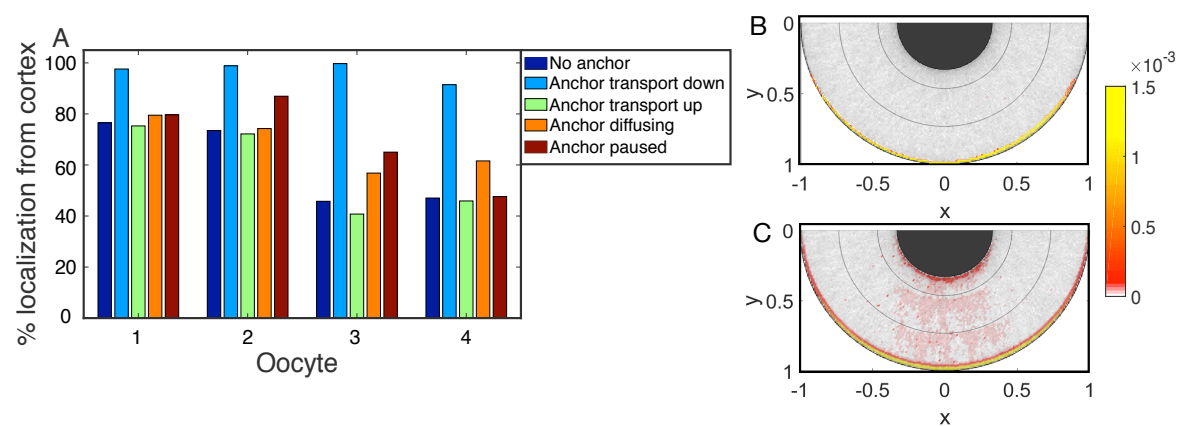


Figure 8. (A) Predicted fraction of localization at 24 hours of simulation; each of the four mRNA states is fully anchored within 5% of the vegetal cortex for parameters from four sample oocytes. The dark blue bar of oocyte 1 corresponds to the RNA distribution illustrated in Figure 6(B). (B) Predicted mRNA localization distribution at 24 hours under anchoring of the transport down state (light blue bar for oocyte 1). (C) Predicted mRNA localization distribution at 24 hours under anchoring of the transport up state (green bar for oocyte 1). The color bar from Figure 5 is included.

anchor any particular state (transport down, transport up, diffusing, or paused) by setting the reaction rates out of the chosen state to 0 in the anchoring region. For example, setting rates $\gamma_+ = \delta_+ = 0$ (equations (38) and [10, Figure 3B]) next to the vegetal cortex is equivalent to allowing particles to be transported down in this region, but once they reach this state they cannot transition to the diffusion or paused state and are therefore anchored with the attached motor proteins. Figure 8 shows the results of anchoring each state in the 4-state model for simulations of four sample individual oocytes with their corresponding parameter estimates from [10]. While the percentage of localized mRNA increases to some extent when anchoring the paused or diffusing states, Figure 8 clearly suggests that anchoring of the transport down state is most efficient in guaranteeing complete or almost complete localization of mRNA.

These results indicate that anchoring at the cell cortex may depend on stabilization of cargo that is likely actively delivered by molecular motors to the vegetal pole. This hypothesis is supported by experiments in [17, Figure S8], where the motor proteins are found to colocalize with Vg1 RNA at the vegetal cortex 24 hours into localization. While dynein and kinesin motors are hypothesized to be primarily responsible for RNA transport in the upper and lower vegetal cytoplasm in *Xenopus* oocytes [17], our results suggest that an active movement state potentially involving molecular motors may be involved in anchoring of mRNA in this system.

Time-dependent anchoring of mRNA captures the spatial distribution of localization. Figure 8 shows the percentage of mRNA localized 24 hours into localization, yet it does not reveal the dynamics throughout the process. Figure 7(B) illustrates that allowing complete anchoring of the transport down state (light blue bars in Figure 8) leads to localization of 90% of mRNA particles in less than 8 hours, which is faster than observed in experiments [17]. Therefore, in addition to pointing to a necessary anchoring mechanism in the vegetal cortex, another potential insight from our simulations is that the transition rates in this anchoring region may

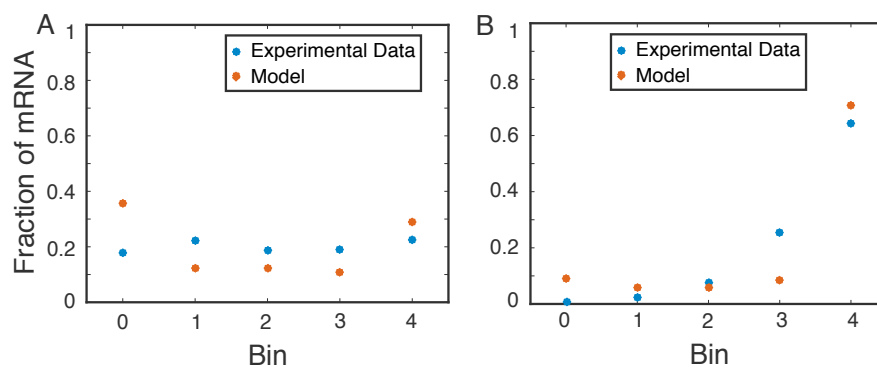


Figure 9. Comparison of the amount of mRNA localized at 10 (A), respectively, 24 (B) hours in each radial spatial bin (bin 0 is closest to the nucleus, and bin 4 is closest to the vegetal cortex).

depend on the amount of mRNA already localized, which may open up more binding sites for anchoring additional mRNA and varies with time [24,30].

A simple test of this hypothesis is to consider transition rates that vary with time in our simulations. In particular, we allow the rates out of the transport down state (δ_+ , γ_+) to decrease smoothly from the estimated values for the lower cytoplasm region in [10] to 0, so that this transport state progresses towards complete anchoring. In addition, we also vary rates β_- and α_- from values an order of magnitude larger than estimated in [10] to their original values, thus allowing for potential recycling of motor proteins so that they can transport additional cargo to the vegetal cortex. We compare our simulations to measures of mRNA content that we extract from experimental images 10 and 24 hours into localization [17, Figure S2] in each spatial annulus around the oocyte nucleus (as described in section 3.2). This time-dependent rate scenario provides the best fit of our simulation results to these measurements of mRNA content from experimental images, as illustrated in Figure 9. The progression towards complete anchoring in these transition rates also influences the timescale of localization (see Figure 7(C)) in our model simulations.

4. Conclusions. The present work proposes models of intracellular transport that take into account the microtubule networks along which molecular motor proteins transport various proteins and vesicles. We carry out a theoretical analysis of linear partial differential equations that model concentrations of cargo which can diffuse, pause, or move bidirectionally with space-dependent velocities on a network of parallel microtubules (with space-dependent densities) and determine explicit expressions for effective velocity and diffusion rates for the modeled particles at large times. Numerical simulations building on these theoretical results show that randomly distributed microtubules lead to higher effective diffusion (spread) of cargo, thus indicating that realistic microtubule cytoskeletons should be used in mRNA transport models. Compared with prior theoretical work [8,23], our theoretical analysis is not restricted to small diffusion and fast reaction rates, as these assumptions may not hold in biological applications as considered here.

We therefore consider a previously validated model [10] of mRNA transport in *Xenopus laevis* oocytes along microtubules with experimentally informed geometries. Specifically, we

carry out numerical simulations as in [48] of a model that combines diffusion of mRNA in the cell, transport along a discrete microtubule network with orientations and densities as observed in *Xenopus* oocytes, and possible anchoring mechanisms at the cortex (with parameters estimated from FRAP microscopy data in [10]). Our results reproduce experimentally observed localization patterns and indicate that anchoring is needed to reproduce the biological timescales.

Our approach to modeling motor-driven transport of mRNA in *Xenopus* oocytes, as well as previous modeling efforts [8, 23, 48], assume that molecular motors are available in unlimited supply in the cytoplasm of oocytes at this stage. By including the microtubule cytoskeleton into our models, we are accounting for spatial binding and unbinding of mRNA to the filaments, and are assuming that molecular motors would be available to transport the mRNA once the particles switch to a moving state. While there is no definite experimental evidence, mRNA transport may be rate-limited by the number of kinesin and dynein motors in the cytoplasm. This would explain the need for models that account for bidirectional transport (such as equations (38)). Interactions between cytoplasmic dynein and kinesin have been identified in an array of systems, with mechanisms for interaction of these opposite polarity motors ranging from “tug-of-war” to regulated coordination, as well as roles in motor recycling [3, 6, 9, 13, 22, 25, 26, 28, 34, 35, 51, 52]. Since complete localization of mRNA is key to development of the frog embryo, bidirectional transport may ensure that dynein (and/or kinesin) can fully explore the cytoplasm of the cell while searching for cargo. Including motor availability into these transport models would lead to useful mathematical models that avoid the challenging problem of estimating transition rates for mRNA bound to various numbers (and types) of motors, as these rates are largely unknown.

Acknowledgments. We are grateful to Dr. Raymond Goldstein for providing the polymer microtubule and transport simulation code used in [48] that we subsequently modified for our application. Part of this research was conducted using computational resources and services at the Center for Computation and Visualization at Brown University and at the Ohio Supercomputer Center through the Mathematical Biosciences Institute at The Ohio State University.

REFERENCES

- [1] V. B. ALARCÓN AND R. P. ELINSON, *RNA anchoring in the vegetal cortex of the Xenopus oocyte*, J. Cell Sci., 114 (2001), pp. 1731–1741.
- [2] K. BABU, Y. CAI, S. BAHRI, X. YANG, AND W. CHIA, *Roles of Bifocal, Homer, and F-actin in anchoring Oskar to the posterior cortex of Drosophila oocytes*, Genes & Develop., 18 (2004), pp. 138–143.
- [3] E. BANANIS, S. NATH, K. GORDON, P. SATIR, R. J. STOCKERT, J. W. MURRAY, AND A. W. WOLKOFF, *Microtubule-dependent movement of late endocytic vesicles in vitro: Requirements for dynein and kinesin*, Molecular Biol. Cell, 15 (2004), pp. 3688–3697.
- [4] B. E. BECKER AND D. L. GARD, *Visualization of the cytoskeleton in Xenopus oocytes and eggs by confocal immunofluorescence microscopy*, in *Xenopus Protocols*, Springer, 2006, pp. 69–86.
- [5] C. BOUZIGUES, M. MOREL, A. TRILLER, AND M. DAHAN, *Asymmetric redistribution of GABA receptors during GABA gradient sensing by nerve growth cones analyzed by single quantum dot imaging*, Proc. Natl. Acad. Sci. USA, 104 (2007), pp. 11251–11256.
- [6] R. P. BRENDZA, L. R. SERBUS, W. M. SAXTON, AND J. B. DUFFY, *Posterior localization of dynein and dorsal-ventral axis formation depend on kinesin in Drosophila oocytes*, Current Biol., 12 (2002),

- pp. 1541–1545.
- [7] P. C. BRESSLOFF AND J. M. NEWBY, *Quasi-steady-state analysis of two-dimensional random intermittent search processes*, Phys. Rev. E, 83 (2011), 061139.
 - [8] P. C. BRESSLOFF AND B. XU, *Stochastic active-transport model of cell polarization*, SIAM J. Appl. Math., 75 (2015), pp. 652–678, <https://doi.org/10.1137/140990358>.
 - [9] A. R. CHAUDHARY, F. BERGER, C. L. BERGER, AND A. G. HENDRICKS, *Tau directs intracellular trafficking by regulating the forces exerted by kinesin and dynein teams*, Traffic, 19 (2018), pp. 111–121.
 - [10] V. CIOCANEL, J. A. KREILING, J. A. GAGNON, K. L. MOWRY, AND B. SANDSTEDE, *Analysis of active transport by fluorescence recovery after photobleaching*, Biophys. J., 112 (2017), pp. 1714–1725.
 - [11] R. DELANOUE AND I. DAVIS, *Dynein anchors its mRNA cargo after apical transport in the Drosophila blastoderm embryo*, Cell, 122 (2005), pp. 97–106.
 - [12] R. DELANOUE, B. HERPERS, J. SOETAERT, I. DAVIS, AND C. RABOUILLE, *Drosophila squid/hnRNP helps dynein switch from a gurken mRNA transport motor to an ultrastructural static anchor in sponge bodies*, Develop. Cell, 13 (2007), pp. 523–538.
 - [13] N. D. DERR, B. S. GOODMAN, R. JUNGSMANN, A. E. LESCHZINER, W. M. SHIH, AND S. L. RECK-PETERSON, *Tug-of-war in motor protein ensembles revealed with a programmable DNA origami scaffold*, Science, 338 (2012), pp. 662–665.
 - [14] C. ELISCOVICH AND R. H. SINGER, *RNP transport in cell biology: The long and winding road*, Current Opinion Cell Biol., 45 (2017), pp. 38–46.
 - [15] A. FRIEDMAN AND H. BEI, *Uniform convergence for approximate traveling waves in linear reaction-hyperbolic systems*, Indiana Univ. Math. J., 56 (2007), pp. 2133–2158.
 - [16] A. FRIEDMAN AND G. CRACIUN, *Approximate traveling waves in linear reaction-hyperbolic equations*, SIAM J. Math. Anal., 38 (2006), pp. 741–758, <https://doi.org/10.1137/050637947>.
 - [17] J. A. GAGNON, J. A. KREILING, E. A. POWRIE, T. R. WOOD, AND K. L. MOWRY, *Directional transport is mediated by a dynein-dependent step in an RNA localization pathway*, PLOS Biol., 11 (2013), e1001551.
 - [18] S. GANGULY, L. S. WILLIAMS, I. M. PALACIOS, AND R. E. GOLDSTEIN, *Cytoplasmic streaming in drosophila oocytes varies with kinesin activity and correlates with the microtubule cytoskeleton architecture*, Proc. Natl. Acad. Sci. USA, 109 (2012), pp. 15109–15114.
 - [19] D. L. GARD, *Organization, nucleation, and acetylation of microtubules in Xenopus laevis oocytes: A study by confocal immunofluorescence microscopy*, Develop. Biol., 143 (1991), pp. 346–362.
 - [20] D. L. GARD, B. J. CHA, AND E. KING, *The organization and animal-vegetal asymmetry of cytokeratin filaments in stage VI Xenopus oocytes is dependent upon F-actin and microtubules*, Develop. Biol., 184 (1997), pp. 95–114.
 - [21] M. K. GARDNER, M. ZANIC, C. GELL, V. BORMUTH, AND J. HOWARD, *Depolymerizing kinesins Kip3 and MCAK shape cellular microtubule architecture by differential control of catastrophe*, Cell, 147 (2011), pp. 1092–1103.
 - [22] S. P. GROSS, M. A. WELTE, S. M. BLOCK, AND E. F. WIESCHAUS, *Coordination of opposite-polarity microtubule motors*, J. Cell Biol., 156 (2002), pp. 715–724.
 - [23] R. J. HAWKINS, O. BENICHO, M. PIEL, AND R. VOITURIEZ, *Rebuilding cytoskeleton roads: Active-transport-induced polarization of cells*, Phys. Rev. E, 80 (2009), 040903.
 - [24] J. HEASMAN, O. WESSELY, R. LANGLAND, E. J. CRAIG, AND D. S. KESSLER, *Vegetal localization of maternal mRNAs is disrupted by VegT depletion*, Develop. Biol., 240 (2001), pp. 377–386.
 - [25] A. G. HENDRICKS, E. L. HOLZBAUR, AND Y. E. GOLDMAN, *Force measurements on cargoes in living cells reveal collective dynamics of microtubule motors*, Proc. Natl. Acad. Sci. USA, 109 (2012), pp. 18447–18452.
 - [26] A. G. HENDRICKS, E. PERLSON, J. L. ROSS, H. W. SCHROEDER III, M. TOKITO, AND E. L. HOLZBAUR, *Motor coordination via a tug-of-war mechanism drives bidirectional vesicle transport*, Current Biol., 20 (2010), pp. 697–702.
 - [27] N. HIROKAWA AND R. TAKEMURA, *Molecular motors and mechanisms of directional transport in neurons*, Nature Rev. Neurosci., 6 (2005), pp. 201–214.
 - [28] J. JANUSCHKE, L. GERVAIS, S. DASS, J. A. KALTSCHMIDT, H. LOPEZ-SCHIER, D. S. JOHNSTON, A. H. BRAND, S. ROTH, AND A. GUICHET, *Polar transport in the Drosophila oocyte requires Dynein and Kinesin I cooperation*, Current Biol., 12 (2002), pp. 1971–1981.

- [29] S. JESCHONEK, *ImageJ Macro*, available at <https://github.com/sjeschonek>.
- [30] M. KLOC AND L. D. ETKIN, *Delocalization of Vg1 mRNA from the vegetal cortex in Xenopus oocytes after destruction of Xlsirt RNA*, *Science*, 265 (1994), pp. 1101–1103.
- [31] M. KLOC AND L. D. ETKIN, *Two distinct pathways for the localization of RNAs at the vegetal cortex in Xenopus oocytes*, *Development*, 121 (1995), pp. 287–297.
- [32] M. KLOC, K. WILK, D. VARGAS, Y. SHIRATO, S. BILINSKI, AND L. D. ETKIN, *Potential structural role of non-coding and coding RNAs in the organization of the cytoskeleton at the vegetal cortex of Xenopus oocytes*, *Development*, 132 (2005), pp. 3445–3457.
- [33] M. W. KLYMKOWSKY, L. A. MAYNELL, AND C. NISLOW, *Cytokeratin phosphorylation, cytoke-
ratin filament severing and the solubilization of the maternal mRNA Vg1*, *J. Cell Biol.*, 114 (1991), pp. 787–797.
- [34] V. LEVI, A. S. SERPINSKAYA, E. GRATTON, AND V. GELFAND, *Organelle transport along microtubules in Xenopus melanophores: Evidence for cooperation between multiple motors*, *Biophys. J.*, 90 (2006), pp. 318–327.
- [35] L. A. LIGON, M. TOKITO, J. M. FINKLESTEIN, F. E. GROSSMAN, AND E. L. HOLZBAUR, *A direct interaction between cytoplasmic dynein and kinesin I may coordinate motor activity*, *J. Biol. Chem.*, 279 (2004), pp. 19201–19208.
- [36] C. MEDIONI, K. MOWRY, AND F. BESSE, *Principles and roles of mRNA localization in animal development*, *Development*, 139 (2012), pp. 3263–3276.
- [37] T. J. MESSITT, J. A. GAGNON, J. A. KREILING, C. A. PRATT, Y. J. YOON, AND K. L. MOWRY, *Multiple kinesin motors coordinate cytoplasmic RNA transport on a subpopulation of microtubules in Xenopus oocytes*, *Develop. Cell*, 15 (2008), pp. 426–436.
- [38] R. MILO AND R. PHILLIPS, *Cell Biology by the Numbers*, Garland Science, 2016.
- [39] J. NEWBY AND P. C. BRESSLOFF, *Random intermittent search and the tug-of-war model of motor-driven transport*, *J. Statist. Mech. Theory Exper.*, 2010 (2010), P04014.
- [40] J. M. NEWBY AND P. C. BRESSLOFF, *Quasi-steady state reduction of molecular motor-based models of directed intermittent search*, *Bull. Math. Biol.*, 72 (2010), pp. 1840–1866.
- [41] E. A. POWRIE, M.-V. CIOCANEL, J. A. KREILING, J. A. GAGNON, B. SANDSTEDE, AND K. L. MOWRY, *Using in vivo imaging to measure RNA mobility in Xenopus laevis oocytes*, *Methods*, 98 (2015), pp. 60–65.
- [42] M. C. REED, S. VENAKIDES, AND J. J. BLUM, *Approximate traveling waves in linear reaction-hyperbolic equations*, *SIAM J. Appl. Math.*, 50 (1990), pp. 167–180, <https://doi.org/10.1137/0150011>.
- [43] J. SCHINDELIN, I. ARGANDA-CARRERAS, E. FRISE, V. KAYNIG, M. LONGAIR, T. PIETZSCH, S. PREIBISCH, C. RUEDEN, S. SAALFELD, B. SCHMID ET AL., *Fiji: An open-source platform for biological-image analysis*, *Nature Methods*, 9 (2012), pp. 676–682.
- [44] C. A. SCHNEIDER, W. S. RASBAND, AND K. W. ELICEIRI, *NIH Image to ImageJ: 25 years of image analysis*, *Nature Methods*, 9 (2012), pp. 671–675.
- [45] E. SCHULZE AND M. KIRSCHNER, *Microtubule dynamics in interphase cells.*, *J. Cell Biol.*, 102 (1986), pp. 1020–1031.
- [46] R. SINGH AND A. KUMAR, *Multiplication operators and composition operators with closed ranges*, *Bull. Austral. Math. Soc.*, 16 (1977), pp. 247–252.
- [47] T. TANAKA AND A. NAKAMURA, *Oskar-induced endocytic activation and actin remodeling for anchorage of the Drosophila germ plasm*, *Bioarchitecture*, 1 (2011), pp. 122–126.
- [48] P. K. TRONG, H. DOERFLINGER, J. DUNKEL, D. ST JOHNSTON, AND R. E. GOLDSTEIN, *Cortical microtubule nucleation can organise the cytoskeleton of Drosophila oocytes to define the anteroposterior axis*, *eLife*, 4 (2015), e06088.
- [49] P. K. TRONG, J. GUCK, AND R. E. GOLDSTEIN, *Coupling of active motion and advection shapes intracellular cargo transport*, *Phys. Rev. Lett.*, 109 (2012), 028104.
- [50] V. TROVISCO, K. BELAYA, D. NASHCHEKIN, U. IRION, G. SIRINAKIS, R. BUTLER, J. J. LEE, E. R. GAVIS, AND D. ST JOHNSTON, *Bicoid mRNA localises to the Drosophila oocyte anterior by random Dynein-mediated transport and anchoring*, *eLife*, 5 (2016), e17537.
- [51] A. E. TWELVETREES, S. PERNIGO, A. SANGER, P. GUEDES-DIAS, G. SCHIAVO, R. A. STEINER, M. P. DODDING, AND E. L. HOLZBAUR, *The dynamic localization of cytoplasmic dynein in neurons is driven by kinesin-1*, *Neuron*, 90 (2016), pp. 1000–1015.
- [52] R. D. VALE, F. MALIK, AND D. BROWN, *Directional instability of microtubule transport in the presence*

- of kinesin and dynein, two opposite polarity motor proteins*, J. Cell Biol., 119 (1992), pp. 1589–1596.
- [53] N. F. VANZO AND A. EPHRUSSI, *Oskar anchoring restricts pole plasm formation to the posterior of the Drosophila oocyte*, Development, 129 (2002), pp. 3705–3714.
- [54] K. VERSTEEG AND W. MALALASEKERA, *An Introduction to Computational Fluid Dynamics: The Finite Volume Method*, Pearson, 2007.
- [55] J. K. YISRAELI, *VICKZ proteins: A multi-talented family of regulatory RNA-binding proteins*, Biol. Cell, 97 (2005), pp. 87–96.
- [56] J. K. YISRAELI, S. SOKOL, AND D. MELTON, *A two-step model for the localization of maternal mRNA in Xenopus oocytes: Involvement of microtubules and microfilaments in the translocation and anchoring of Vg1 mRNA*, Development, 108 (1990), pp. 289–298.
- [57] W.-M. ZHAO, C. JIANG, T. T. KROLL, AND P. W. HUBER, *A proline-rich protein binds to the localization element of Xenopus Vg1 mRNA and to ligands involved in actin polymerization*, EMBO J., 20 (2001), pp. 2315–2325.
- [58] V. L. ZIMYANIN, K. BELAYA, J. PECREAU, M. J. GILCHRIST, A. CLARK, I. DAVIS, AND D. ST JOHNSTON, *In vivo imaging of oskar mRNA transport reveals the mechanism of posterior localization*, Cell, 134 (2008), pp. 843–853.